Draft, 10 December 2008

Parton propagation and fragmentation at the EIC

Alberto Accardi[1,2], Raphaël Dupré[3,4] and Kawtar Hafidi[3,2]

[1] Hampton University, Hampton, VA, 23668, USA
[2] Jefferson Lab, Newport News, VA 23606, USA
[3] Physics Division, Argonne National Laboratory, Argonne, IL, USA
[4] Université Claude Bernard Lyon 1, Villeurbanne, France

Contents

1 Introduction **2**
1.1 Parton fragmentation in elementary collisions 2
1.2 Parton propagation and hadronization in cold and hot QCD matter 4
1.3 Hadronisation and colour confinement 5
1.4 Hadronisation and neutrino oscillations 6

2 Kinematics and observables **6**
2.1 Kinematic Variables 6
2.2 Comparison of hadron-hadron and DIS kinematics 11
2.3 Nuclear modification observables 16

3 Space-time evolution of hadronisation **17**

4 Short review of fixed target experiments **21**

5 EIC capabilities **22**

6 Simulations **23**
6.1 Method 23
6.2 Detection 24
6.3 Results 25

1 Introduction

The transition from coloured partons (quarks and gluons) to colourless hadrons – the so-called fragmentation or hadronisation process – is an exemplary process of the fundamental theory of the strong interaction, Quantum Chromo-Dynamics (QCD), which still lacks a quantitative understanding from first principles calculations. The process by which a highly virtual parton radiates gluons or splits into a quark-antiquark pair can be theoretically described by the QCD (DGLAP) evolution equations [1–3]. However, the final "bleaching" of partons into a colourless hadron takes place at a low virtualities ($Q \approx \Lambda_{\rm QCD} \approx 0.2$ GeV) and so is dominated by nonperturbative QCD effects which cannot be addressed with the existing perturbative techniques. Modeling and phenomenology – e.g. as implemented in the Lund string [4] or cluster [5] fragmentation approaches – are often used to describe the hadronisation processes.

One way to study hadronisation is to perturb the environment surrounding the hard-scattering short-distance reaction by introducing a nuclear medium [6]. The nuclear medium provides a nontrivial probe of parton evolution through the influence of initial-state (IS) and/or final-state (FS) interactions. Such IS and FS modifications, can help us understand for example the time-scale of the hadronisation process [7]. In the case of large momentum transfer quasi-exclusive reactions, one can use a nuclear target to filter and influence the evolution and structure of the hadron wave-functions themselves.

Nuclear modifications of hadron production have been indeed observed in Deep Inelastic lepton-nucleus Scattering nDIS ($\ell^{\pm} + A$), in hadron-nucleus ($h + A$) and in heavy-ion ($A + A$) collisions, compared to "elementary" proton-DIS or proton-proton collisions. In nDIS and $h + A$ collisions, the medium is the nuclear target itself, also called "cold QCD matter". In $A + A$ reactions, the fragmenting parton must traverse the created hot and dense medium ("hot QCD matter"), be it a hadron gas at low temperature, or a Quark-Gluon Plasma (QGP) at high temperatures. In all cases, at high enough p_T where hadrons mostly come from parton fragmentation, one typically observes two different phenomena: (i) a suppression of hadron multiplicities, called hadron or jet quenching, and (ii) a broadening of hadron transverse momentum spectra, which induces a deformation of the hadron p_T spectrum known as "Cronin effect" [8, 9]. Such nuclear modifications can be attributed to elastic and inelastic interactions of the scattered partons (and/or of the produced hadrons) as well as to modifications of their fragmentation while traversing the surrounding medium.

In nDIS, a well known medium like a target nucleus allows one to test the hadronisation mechanism and colour confinement dynamics. Knowledge of partonic in-medium propagation gained from nDIS can be used in Drell-Yan (DY) lepton pair production in $h + A$ collisions to factor out medium-induced gluon radiation and nuclear modifications of parton distributions. In addition, hadron quenching is also an important source of systematic uncertainty in neutrino oscillation experiments, which use nuclear targets and need to reconstruct the event kinematics from the hadronic final-state. Conversely, a precise knowledge of parton propagation and hadronisation mechanisms obtained from nuclear DIS and DY is essential for testing and calibrating our theoretical tools to determine the properties of the QGP produced in high-energy heavy-ion collisions.

1.1 Parton fragmentation in elementary collisions

In perturbative Quantum Chromodynamics (pQCD), collinear factorisation theorems [10] allow one to explicitly separate the short and long distance QCD dynamics involved in the mechanism of

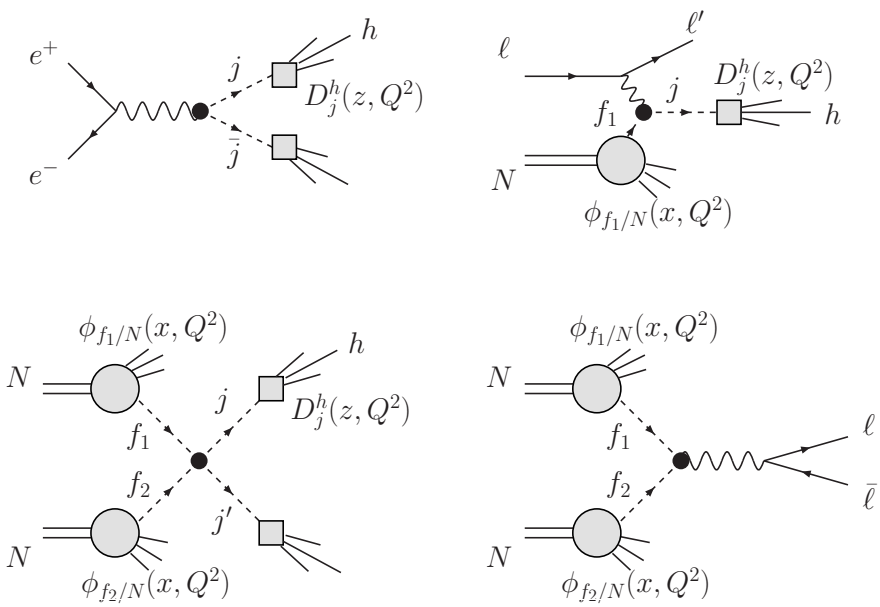

Figure 1: Illustration of universality of PDFs ($\phi_{f/N}$) and FFs ($D_{j\to h}$) in leading order processes. Clockwise from top left: $e^+ + e^-$ annihilation, Deep Inelastic Scattering (DIS), lepton pair (Drell-Yan) emission, and hadron production in hadronic collisions. Solid lines indicate leptons, dashed lines quarks. The small black disc represents the perturbatively calculable hard interaction coefficient $\hat{H}_{\text{partonic}}$.

hadron production from parton fragmentation. In a general inelastic collision $H_1 + \ldots + H_N$, one writes the semi-inclusive hadronic cross sections for production of a hadron h at large, or "hard", scale Q^2 (e.g., a large 4-momentum transfer) as

$$\begin{aligned}&\sigma_{\text{hard}}(H_1 + \ldots + H_N \to h + X)\\ &\quad = \sum_{f_i, j=\{q,g\}} \Big[\prod_{i=1,N} \phi_{f_i/H_i}(x_i, Q^2)\Big] \otimes \hat{H}^{\{f_i\}\to j+X}_{\text{partonic}}(\{x_i\}, z_j, Q^2) \otimes D_{j\to h}(z; Q^2)\,,\end{aligned} \tag{1}$$

where $\otimes$ denotes a convolution over the kinematical internal variables of the process. In Eq. (1), Q^2 is the typical (hard) scale of the process and $\hat{H}_{\text{partonic}}$ is the short-distance and perturbatively calculable hard interaction coefficient for the $\{f_i\}\to j + X$ partonic process. The long-distance dynamics is factorised into (a) the Parton Distribution Functions (PDF) $\phi_{f_i|H_i}(x_i)$, which give the probability of finding a parton of flavor f_i and momentum fraction x_i inside the hadron H_i, and (b) the Fragmentation Function (FF) $D_{j\to h}$, which gives the probability that the parton j fragments into the observed hadron h with fractional momentum z. These functions are non-perturbative and need to be extracted from experimental data. Typically, PDFs are extracted from "global QCD fits" of inclusive hadron production in lepton-nucleon DIS [$N = 1$ and $D_{j\to h}(z; Q^2) = 1$ in Eq. (1)], and FFs from electron-positron annihilation into hadrons [$N = 0$ in Eq. (1)]. The obtained PDFs and FFs are provided by various authors, e.g., CTEQ6.6, MRST/MSTW [11–13] and DSS, AKK08 [14–16]. Once they are known at a given scale Q_0^2 their value at any other scale can be perturbatively computed by means of the DGLAP evolution equations [1–3].

An important consequence of factorisation theorems is that PDFs and FFs are universal: the above measured functions are process-independent. The measured FFs in $e^+ + e^- \to h + X$ and the

PDFs in $e^{\pm} + p \to h + X$ can then be used to compute observables in other process, e.g., hadron spectra in proton-proton collisions [$N = 2$ in Eq. (1)], or Drell-Yan production of lepton pairs [$N = 2$ and $j = \ell\bar{\ell}$ in Eq. (1)], see Fig. 1.

When dealing with hadron production with nuclear systems, universality is experimentally observed to breakdown: the details of the hadron production cross sections depend on the collision process that yields the final particles, as we discuss next.

1.2 Parton propagation and hadronization in cold and hot QCD matter

The basic assumption behind the factorised form of Eq. 1 is that the characteristic time of the parton-parton interaction is much shorter than any long-distance interaction occurring before (among partons belonging to the same PDF) or after (during the evolution of the struck partons into their hadronic final-state) the hard collision itself. In that case, one can treat each nucleus as a collection of free partons, i.e. *in the absence of initial-state effects*, the parton density in a nucleus with mass number A is expected to be simply equivalent to that of a superposition of A independent nucleons: $\phi_{a/A}(x, Q^2) = A \cdot \phi_{a/N}(x, Q^2)$. In addition, *in the absence of final-state effects* the parton fragments in the vacuum with universal FFs and, therefore, the pQCD factorization theorem for collisions involving nuclei A predicts simply:

$$\begin{aligned} \sigma_{hard}(l, h + A \to h + X) &= A\, \sigma_{hard}(l, h + p \to h + X) \\ \sigma_{hard}(A + A \to h + X) &= A^2\, \sigma_{hard}(p + p \to h + X) \end{aligned} \tag{2}$$

The cleanest environment to test the validity of Eq. 2 and study possible nuclear modifications of hadron production is nuclear Deep Inelastic Scattering (nDIS): it allows to experimentally control many kinematic variables; the nuclear medium (i.e., the nucleus itself) is well known; and the particle multiplicity in the final state is low, allowing for precise measurements. The nucleons act as femtometer-scale detectors of the hadronizing quark, allowing one to experimentally study its space-time evolution into the observed hadron(s) (Fig. 2, left). The relevant observable in nDIS processes is the ratio of the single hadron multiplicity on a target of mass number A normalised to the multiplicity on a deuteron target. At leading order, this multiplicity ratio corresponds to the ratio of fragmentation functions (FF) in "cold nuclear matter" (the nucleus A) over that in the "vacuum" (deuteron). Recent HERMES measurements show a significant reduction of this ratio [17–20], clearly showing a breakdown of universality for fragmentation functions.

A complementary means to study parton propagation in cold QCD matter is by measuring the Drell-Yan (DY) process in hadron-nucleus collisions: $h + A \to \ell^+\ell^- + X$ (Fig. 2, center). If the invariant mass of the lepton pair is large, the process can be described perturbatively as a parton-parton scattering producing a vector boson which subsequently decays into the lepton pair. Any modifications of this process compared to A times the cross sections measured in hadron-hadron collisions will come from initial-state nuclear interactions of the projectile parton inside the target (as well as from nuclear modifications of the PDF, which can be isolated by other means).

Tests of pQCD factorisation in hot-dense QCD matter can be carried out studying high-p_T hadron production in head-on nucleus-nucleus reactions (Fig. 2, right). The suppression of large transverse momentum hadron production in $A + A$ compared to proton-proton ($p + p$) and hadron-nucleus $h + A$ collisions at RHIC [21–24], is also indicative of a breakdown of the universality of the fragmentation process. The standard explanation is that the observed suppression is due to

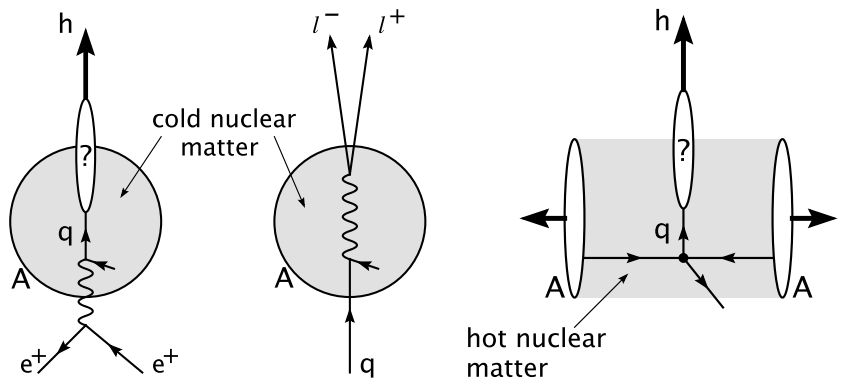

Figure 2: Quark propagation inside a target nucleus ("cold QCD matter") in lepton-nucleus (left) and hadron-nucleus → Drell-Yan (center) collisions. Right: Hard scattered parton traveling through the "hot QCD matter" produced in a nucleus-nucleus collision.

parton energy loss in the strongly interacting matter. This assumes of course that the quenched light-quarks and gluons are long-lived enough to traverse the medium before hadronizing, which is a reasonably assumption at high enough p_T. If, on the contrary, hadronisation started at the nuclear radius scale or before, in-medium hadron interactions should also be accounted for, possibly leading to a different suppression pattern. Such a mechanisms may be at work, for example, in the case of heavy (charm, bottom) quarks which – being slower than light-quarks or gluons – can fragment into D or B mesons still inside the plasma [25].

In summary, a precise knowledge of parton propagation and hadronisation mechanisms can be obtained from nDIS and DY data, allowing one to test the hadronisation mechanism and colour confinement dynamics. In addition, such cold-nuclear matter data are essential for testing and calibrating our theoretical tools, and to determine the properties of the QGP produced in high-energy nuclear interactions.

1.3 Hadronisation and colour confinement

While not having a direct bearing on the traditional topics of confinement such as the hadron spectrum and the value of infrared cutoffs in hadron structure, the hadronisation process nonetheless contains elements that are central to the heart of colour confinement, as already emphasised 30 years ago by Bjorken [6]. For instance, in the DIS process, a quark is briefly liberated from being associated with any specific hadron while traveling as a 'free' particle, and it is the mechanisms involved in hadron formation that enforces the colour charge neutrality and confinement into the final state hadron. The dynamic mechanism leading to colour neutralisation, which is only implicitly assumed in the traditional treatments of confinement based on potential models [26] or lattice QCD [27], can be studied quantitatively using the theoretical and experimental techniques discussed in this review. As an example, the lifetime of the freely propagating quark can be inferred experimentally from the partonic multiple scattering process in cold nuclei, which act as femtometer-scale detectors of the hadronisation process. Finally, as already discussed, the behaviour of quarks propagating through the medium created in high energy heavy-ion collisions can give insight into, and measure, the properties of large-scale deconfined QCD matter (i.e., of the Quark-Gluon Plasma). While still at an early stage, the understanding of such elements will

ultimately provide deeper insights into the confinement-related properties of QCD.

1.4 Hadronisation and neutrino oscillations

Neutrino oscillation experiments use nuclear targets to enhance the neutrino detection rate. Nuclear effects change the topology and total energy of the hadronic final state. The systematic error describing how well these nuclear effects are known is one of the largest systematic errors in current analyses. For the lower energy oscillation experiments that use the quasi-elastic channel as their signal, there are several problems including the distortion of the knock-out nucleon due to final state interactions, the contamination from hadron resonances, e.g. the $\pi + N \to \Delta$ process by which a final-state pion is absorbed in the nucleus, and the mainly unexplained depletion of low-virtuality events, much stronger than Pauli blocking can account for [28]. Experiments such as MINOS measure the neutrino energy adding up the muon and hadronic energies, $E_\nu = E_\mu + E_{\rm had}$. It is thus crucial to have a good understanding of hadron modifications in the nuclear medium and of the space-time evolution of the hadronisation process [29, 30]. However, at the low hadronic invariant mass involved in these experiments the theoretical methods discussed in this review should be supplemented by those described in Refs. [31–34].

2 Kinematics and observables

In this Section the kinematic variables and observables for nDIS, and compare them to hadronic collisions in terms of their phase spaces for hadron production.

2.1 Kinematic Variables

Throughout this discussion we use light-cone coordinates: for any 4-vector a^μ we write $a^\mu = (a^+, a^-, \vec{a}_T)$, where $a^\pm = (a^0 \pm a^3)/\sqrt{2}$ are the plus- and minus-momenta and $\vec{a}_T = (a^1, a^2)$ the transverse momentum. Our reference frame is such that the z axis is aligned with the beam, and a particle moving in the positive z direction has large light-cone plus-momentum. The transverse plane is the plane transverse to the beam. The dot product is $a \cdot b = a^+ b^- + a^- b^+ - \vec{a}_T \cdot \vec{b}_T$, and $p^+ p^- = m^2 + p_T^2 \equiv m_T^2$, where $m^2 = p^2$ is the invariant mass of the particle, and m_T its transverse mass. A longitudinal boost of velocity β along the 3-direction acts multiplicatively on the plus- and minus-components:

$$p'^+ = \alpha p^+ \qquad p'^- = \frac{1}{\alpha} p^- \ , \tag{3}$$

where $\alpha = \sqrt{(1-\beta)/(1+\beta)}$. As an example, let us boost the target hadron momentum P from the target rest frame, $P = (M/\sqrt{2}, M/\sqrt{2}, \vec{0}_T)$, to a frame in which $P' = (\sqrt{s/2}, M^2/\sqrt{2s}, \vec{0}_T)$. This boost is accomplished by $\alpha = \sqrt{s}/M$. Likewise, boosting a nucleon from energy $\sqrt{s}/2$ to $\sqrt{s'}/2$ requires $\alpha = \sqrt{s'/s}$.

Deep inelastic scattering at LO in pQCD proceeds by exchange of a virtual photon in the $\hat{t}$-channel (Fig. 3 left). The DIS Lorentz invariants are defined in Table 1. Note that the variable x_B, Q^2 and ν are not independent but related by $x_B = Q^2/(2M\nu)$ in any reference frame. Semi-inclusive nDIS is best discussed in terms of ν and Q^2, which are the most relevant variables to

Variable	*Definition*	*Target rest frame form*	
$\boldsymbol{M^2}$	$= P^2$		Target mass.
$\boldsymbol{x_B}$	$= \frac{-q^2}{2P\cdot q}$		Bjorken scaling variable.
$\boldsymbol{Q^2}$	$= -q^2$		Negative four-momentum squared of the virtual photon.
$\boldsymbol{\nu}$	$= \frac{q\cdot P}{\sqrt{P^2}}$	$= E_e^{trf} - E_e^{trf\prime}$	Energy of the virtual photon in the target rest frame.
$\boldsymbol{y}$	$= \frac{q\cdot P}{k\cdot P}$	$= \frac{\nu}{E_e^{trf}}$	Fractional energy loss of the incident lepton (inelasticity).
$\boldsymbol{W^2}$	$= (P+q)^2$	$= M^2 + 2M\nu - Q^2$	Invariant mass squared of the hadronic final state.
$\boldsymbol{z_h}$	$= \frac{p_h\cdot P}{q\cdot P}$	$= \frac{E_h}{\nu}$	Fraction of the virtual photon energy carried by the hadron.
$\boldsymbol{p_T}$	$= \lvert\vec{p}_T\rvert$		Hadron transverse momentum (relative to the virtual photon momentum).

Table 1: Definitions of the kinematic variables for semi-inclusive DIS. The Lorentz invariant definition and its form in the target rest frame are provided. Particle 4-momenta are defined in Fig. 3 and 4. All variables are experimentally measurable, hence typeset in boldface. Note that $x_B = Q^2/(2M\nu)$ independently of the chosen reference frame.

hadron quenching processes in nuclear targets. Analysis of inclusive DIS is usually carried out using x_B and Q^2, because to leading order the cross section scales in x_B. Note that in DIS one can experimentally measure all the listed variables, especially ν, Q^2 and z_h, because the initial and final state electron is observable. This is markedly different from the situation in hadronic collisions, where only the final state hadrons can be observed, not the partons themselves. The hadron transverse momentum in DIS is defined with respect to the photon direction, see Fig. 4. Its analog in hadronic collisions would be the transverse momentum of a hadron with respect to the jet axis.

DIS experiments have been performed in fixed-target (*ft*) conditions in facilities like SLAC (E665), SPS (EMC), DESY (HERMES), JLab (CLAS); or in collider mode (*cl*) e.g. at the proposed Electron-Ion Collider (EIC) or Large Hadron-electron Collider (LHeC). The colliding nucleon and lepton momenta are

$$\begin{aligned} P_{ft} &= \left(\frac{M}{\sqrt{2}}, \frac{M}{\sqrt{2}}, \vec{0}_T\right), \quad k_{ft} = \left(\sqrt{2}E_e, 0, \vec{0}_T\right) \\ P_{cl} &= \left(\frac{M}{2\sqrt{2}E_N}, \sqrt{2}E_N, \vec{0}_T\right), \quad k_{cl} = \left(\sqrt{2}E_e, 0, \vec{0}_T\right) \end{aligned} \tag{4}$$

where E_e and E_N are the electron and nucleon energies measured in the laboratory frame. To discuss both modes at the same time, it is convenient to introduce the target rest frame energy of

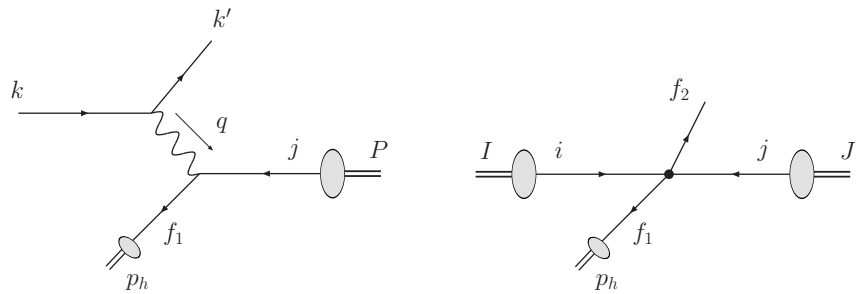

Figure 3: LO kinematics for parton production in DIS collisions (*left*) and in hadron-hadron collisions (*right*). Double lines indicate hadrons or nuclei, thin single lines are partons or leptons. The labels define the particles 4-momenta.

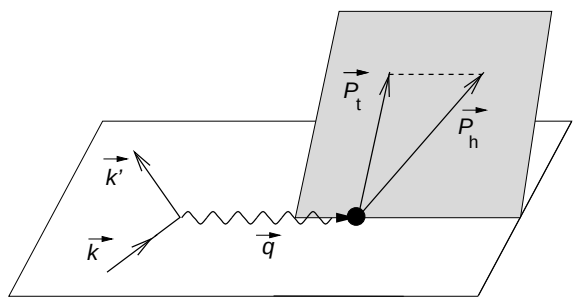

Figure 4: Kinematic planes for hadron production in semi-inclusive deep-inelastic scattering and definitions of the relevant lepton and hadron variables. The quantities k (k') and E (E')are the 4-momentum and the energy of the incident (scattered) positron; p_h is the 4-momentum of the produced hadron, and its transverse component relative to the lepton plane is denoted by $\vec{p}_T$.

the electron,E_{trf}:

$$E_{trf} = \begin{cases} E_e & \text{fixed-target} \\ \frac{2E_N E_e}{M} & \text{collider mode} \end{cases} \tag{5}$$

Then the invariant inelasticity y for both modes can be written as $y = \nu/E_{trf}$.

Next, we consider parton production at colliders. To be general, let us discuss hadron-hadron collisions: lepton-hadron collisions can be obtained as a special case whereas the incident lepton itself is considered a parton with well definite fractional momentum, see Fig. 3 and Sect. 2.2. At leading order in the coupling constant α_s partons are produced by 2→2 partonic collisions. The relevant kinematic variables are defined in Table 2. Several LO processes can contribute to a given $ij \to f_1 f_2$ collision, represented by a black dot in the cartoon, see Ref. [35] for details. The momenta of the two nucleons colliding in the center-of-mass-frame (c.m.f.) with energy $\sqrt{s}/2$ each are

$$I = \left(\sqrt{\frac{\tilde{s}}{2}}, \frac{M^2}{\sqrt{2\tilde{s}}}, \vec{0}_T\right) \qquad J = \left(\frac{M^2}{\sqrt{2\tilde{s}}}, \sqrt{\frac{\tilde{s}}{2}}, \vec{0}_T\right) \tag{6}$$

Variable		*Definition*	
$\boldsymbol{s}$			Nucleon-nucleon center of mass energy squared.
x_1	=	i^+/I^+	Initial-state projectile parton fractional momentum.
x_2	=	j^-/J^-	Initial-state target parton fractional momentum.
p_{iT}	=	$\lvert\vec{f}_{iT}\rvert$	Final state partons transverse momentum (relative to beam).
y_i	=	$0.5\log(f_i^+/f_i^-)$	Final state partons rapidity.
$\boldsymbol{y_{cm}}$	=	$0.5\log(\frac{I^++J^+}{I^-+J^-})$	Rapidity of the center of mass.
z	=	p_h^+/f_1^+	Hadron fractional momentum relative to parent parton f_1.
$\boldsymbol{p_{hT}}$	=	$\lvert\vec{p}_{hT}\rvert$	Hadron transverse momentum (relative to beam).
$\boldsymbol{y_h}$	=	$0.5\log(p_h^+/p_h^-)$	Hadron rapidity.
$\boldsymbol{\eta}$	=	$-\log\tan(\theta^*/2)$	Hadron pseudorapidity (θ^* is the polar angle between the parton and the beam in the center of mass reference frame).

Table 2: Relevant kinematic variables for semi-inclusive parton (top) and hadron (bottom) production defined in perturbative QCD. Particle 4-momenta are defined in Fig. 3, right. Boldface variables are experimentally measurable. Note that at LO, with two final state partons, $\vec{p}_{1T} = -\vec{p}_{2T} = \vec{p}_T$.

where M is the nucleon mass and

$$\tilde{s} = s\frac{1+\sqrt{1+M^4/s^2}}{2}\,. \tag{7}$$

We will neglect terms of order $O(M^2/s)$ compared to terms of $O(1)$, and will use $\tilde{s} \approx s$. In Eq. (6), we explicitly retain the nucleon mass to be able to perform boosts to the rest frame of either nucleon. If we assume the partons to be massless and collinear to their parent nucleons, their 4-momenta in terms of the parton fractional momenta x_i read $i = \left(x_1\sqrt{s}/2, 0, \vec{0}_T\right)$ and $j = \left(0, x_2\sqrt{s}/2, \vec{0}_T\right)$.

Particle production (partons or hadrons) is described in terms of the particle rapidity and transverse momentum. The rapidity of a particle of 4-momentum p and mass $m^2 = p^2$ is defined as

$$y = \frac{1}{2}\log\left(\frac{p^+}{p^-}\right) = \log\left(\frac{p^+}{m_T}\right). \tag{8}$$

The rapidity may be either positive or negative, and describes a particle moving in the positive or negative z direction, respectively. Under a longitudinal boost of velocity β, the rapidity transforms additively: $y' = y - y_\beta$, where $y_\beta = 0.5\log[(1+\beta)(1-\beta)]$ is the rapidity of the particle rest frame. In the non-relativistic limit the rapidity coincides with the particle longitudinal velocity v measured in units of the speed of light, $y \to v$. This fact and the transformation laws just discussed justify considering the rapidity as the relativistic generalisation of the velocity of a particle. Given the rapidity, one can compute $p^0 = m_T\cosh y$ and $p^3 = m_T\sinh y$.

Measuring the rapidity of a particle requires measuring two independent variables, say, its energy and longitudinal momentum. Not in all experiments this is possible, while just measuring

the polar angle θ^* between the particle trajectory and the beam axis in the center of mass frame is easier. This justifies the definition of the particle pseudorapidity,

$$\eta = -\log\tan(\theta^*/2)\,, \tag{9}$$

such that $|\vec{p}| = p_T \cosh\eta$ and $p^3 = p_T \sinh\eta$. For massless particles it coincides with the rapidity: $\eta = y$; for massive particles, they are approximately equal if $|\vec{p}| \gg m$ (and $\theta \gg 0$). Differential particle distributions in y and η are related by

$$\frac{dN}{dyd^2p_T} = \frac{dN}{d\eta d^2p_T}\sqrt{1-\frac{m^2}{m_T^2\cosh^2 y}} = \frac{dN}{d\eta d^2p_T}\frac{E}{m_T}\,. \tag{10}$$

At LO, the final state parton 4-momenta in terms of the final state rapidities y_i and transverse momentum p_T (see Table 2 for definitions) read

$$f_1 = \left(\frac{p_T}{\sqrt{2}}e^{y_1}, \frac{p_T}{\sqrt{2}}e^{-y_1}, -\vec{p}_T\right) \qquad f_2 = \left(\frac{p_T}{\sqrt{2}}e^{y_2}, \frac{p_T}{\sqrt{2}}e^{-y_2}, \vec{p}_T\right), \tag{11}$$

and their fractional momenta are

$$x_1 = \frac{p_T}{\sqrt{s}}(e^{y_1}+e^{y_2}) \qquad x_2 = \frac{p_T}{\sqrt{s}}(e^{-y_1}+e^{-y_2})\,. \tag{12}$$

Finally, the Mandelstam invariants are defined as follows,

$$\begin{aligned}\hat{s} &= (i+j)^2\\ \hat{t} &= (i-f_1)^2 = (f_2-j)^2\\ \hat{u} &= (i-f_2)^2 = (f_1-j)^2\end{aligned} \tag{13}$$

and 4-momentum conservation for massless partons is expressed as $\hat{s}+\hat{t}+\hat{u} = 0$. In terms of rapidities and transverse momentum, the Mandelstam invariants read

$$\begin{aligned}\hat{s} &= x_1x_2s\\ \hat{t} &= -p_T^2(1+e^{y_2-y_1})\\ \hat{u} &= -p_T^2(1+e^{y_1-y_2})\,.\end{aligned} \tag{14}$$

In order to compare collider and fixed-target experiments, and different beam energies, it is useful to consider the rapidity in the c.m.f.:

$$y_{c.m.f.} = y - y_{cm}\,, \tag{15}$$

where y_{cm} is the rapidity of the center of mass in the lab frame. The backward rapidity region (target hemisphere) corresponds to $y - y_{cm} < 0$, and the forward rapidity region (projectile hemisphere) to $y - y_{cm} > 0$.

Hadronisation in the collinear factorisation framework proceeds through independent parton fragmentation into a hadron. It is universal, i.e., independent of the process which produced the

Variable		*Definition*		LO in α_s	
$\boldsymbol{x_F}$	=	$2p_z^*/\sqrt{s}$	=	$x_1 - x_2$	Feynman x.
$\boldsymbol{M}$	=	$\sqrt{p_{\ell^+}^2 + p_{\ell^-}^2}$	=	$x_1 x_2 s$	Dilepton invariant mass.
$\boldsymbol{p_T}$	=	$\lvert\vec{p}_T\rvert$			Dilepton transverse momentum.

Table 3: Kinematic variables for Drell-Yan dilepton production. The dilepton momentum is $p = p_{\ell^+} + p_{\ell^-}$, where $p_{\ell^\pm}$ are the lepton and anti-lepton momenta. A star indicates momenta measured in the center of mass frame. The 3 DY variables are experimentally measurable, hence typeset in boldface. See Table 2 for the definition of $x_{1,2}$ and s.

fragmenting hadron, e.g., hadronic or DIS collisions [36]. The hadron fractional momentum z is defined by

$$p_h^+ = z f_1^+ \qquad \vec{p}_{hT} = z \vec{f}_{1T} \ . \tag{16}$$

Therefore the on-shell hadron momentum p_h reads

$$p_h = (z f_1^+, \frac{m_h^2 + z^2 f_{1T}^2}{2z f_1^+}, z \vec{f}_{1T}) \ . \tag{17}$$

The parton and hadron rapidities are related by $y_1 = y_h + \log(m_{hT}/p_{hT})$.

The partonic variables p_T, y_i, x_i and the fractional hadron momentum z are not experimentally measurable, but needed in the theoretical computation of the cross section. The experimentally measurable variables are typed in boldface in Table 2. Note that the hadron transverse momentum p_T in hadron-hadron collisions is defined with respect to the beam axis, so that at midrapidity it is the analog of the hadron energy E_h in DIS.

2.2 Comparison of hadron-hadron and DIS kinematics

If we consider parton and hadron production at LO in hadronic and DIS collisions, it is easy to provide an explicit dictionary translating between the relevant variables in both processes, that allows one to compare their corresponding phase spaces. The discussion closely follows Ref. [37], to which we refer for details. To connect the DIS and hadron-hadron kinematics (Fig. 3) we can boost the DIS collision to a frame in which the target has energy $\sqrt{s}/2$ per nucleon. Then, we can imagine the lepton to be a parton of a collinear phantom nucleon of energy $\sqrt{s}/2$ and with 4-momentum $P'^{\pm} = P^{\mp}$. Comparing the left and right parts of Fig. 3 we can identify

$$P \equiv J, \quad P' \equiv I, \quad k \equiv i, \quad k' \equiv f_2. \tag{18}$$

The virtual photon momentum q, the fractional momentum x_e of the initial-state lepton and the rapidity y_e of the final state lepton are identified as follows

$$q = k - k' \equiv i - f_2, \quad x_e = k^+/P'^+ \equiv x_1, \quad y_e \equiv y_2 \ .$$

In this way, we can relate the DIS kinematics to the hadron-hadron kinematics discussed in Sect. 2.1. As an example, it is immediate to see that, in terms of hadron-hadron variables, $Q^2 = -\hat{t}$. The full

	SPS	FNAL	RHIC	RHIC	LHC
$\sqrt{s}$ [GeV]	17.5	27.4	63	200	5500
Δy_1	2.4	2.0	1.2	0	-3.3

Table 4: Rapidity shifts Δy_1 of the RHIC-equivalent DIS phase space, tabulated for some energies of interest.

translation dictionary from DIS to hadron-hadron variables can be obtained in a straightforward way by combining the results of Section 2.1 and the definitions of Tables 1–2.

First, we can express the DIS invariants in terms of parton rapidities and transverse momenta. Neglecting target-mass corrections, i.e. up to terms of $O(M^2/s)$, we obtain

$$\begin{aligned} x_B &= \frac{p_T}{\sqrt{s}}(e^{-y_2} + e^{-y_1}) \\ Q^2 &= p_T^2(1 + e^{y_1 - y_2}) \\ \nu &= \frac{p_T\sqrt{s}}{2M} e^{y_1} \\ y &= \frac{1}{1 + e^{y_2 - y_1}} \\ z_h &= z\ . \end{aligned} \tag{19}$$

Note that the first 3 variables are not independent because $Q^2 = 2Mx_B\nu$, and that $x_B = x_2$ is interpreted as the struck parton fractional momentum, as expected in DIS at LO. Note also that ν increases with increasing p_T and increasing y_1. In other words, a parton of positive and large y_1 travels in the opposite direction as its parent nucleon, hence in the target rest frame it is very fast. Conversely, a parton of negative and large y_1 travels in the same direction as its parent nucleon, which means quite slow in the target rest frame. It is also interesting to note that up to terms of order $O(M^2/s)$, the parton and hadron energy in the target rest frame are $E = \nu$ and $E_h = z_h\nu$ respectively. Finally, we can invert Eq. (19) to obtain the hadron-hadron variables in terms of DIS invariants:

$$\begin{aligned} p_T^2 &= (1-y)Q^2 \\ y_1 &= -\log\Big(\frac{Q\sqrt{s}}{2ME_{trf}}\,\frac{(1-y)^{1/2}}{y}\Big) \\ y_2 &= y_1 + \log\Big(\frac{1-y}{y}\Big) \\ z &= z_h \end{aligned} \tag{20}$$

with $y = \nu/E_{trf}$. Note that in DIS, the electron energy E_{trf}, hence the electron x_e, is fixed by the experimental conditions; this is different from hadronic collisions where the parton j has an unconstrained fractional momentum. Changing the c.m.f. energy to $\sqrt{s'}$ simply results in a shift of the parton rapidity,

$$y_1 \xrightarrow[s\to s']{} y_1 + \Delta y_1 \tag{21}$$

where $\Delta y_1 = \log(\sqrt{s}/\sqrt{s'})$. The value of Δy_1 compared to RHIC top energy $\sqrt{s_{\rm NN}} = 200$ GeV is listed in Table 4 for the experiments of interest in this paper.

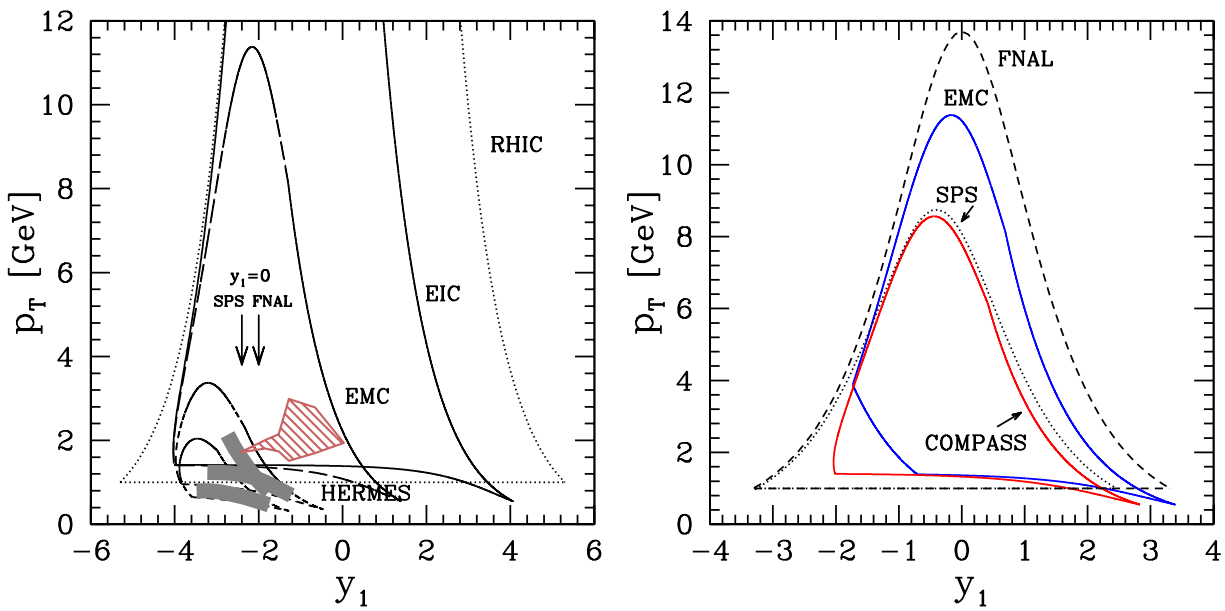

Figure 5: *Left:* the RHIC-equivalent phase space of DIS experiments at $E_e = 27.6$ GeV (HERMES, solid line), at $E_e = 12$ GeV (HERMES and JLab, dashed line), and at $E_e = 280$ GeV (EMC, dot-dashed line). The dotted line shows the borders of the LO pQCD phase space at top RHIC energy, $\sqrt{s_{\rm NN}} = 200$ GeV. The two arrows show the location of the midrapidity region at SPS and FNAL fixed-target experiments. The shaded regions show the region of phase-space experimentally explored at HERMES [19, 38] and EMC [39]. *Right:* hadron-hadron-equivalent EMC and COMPASS phase space at $\sqrt{s_{\rm NN}} = 27.4$ GeV, compared to the SPS and FNAL phase spaces.

Given a DIS phase space, i.e., a given experiment acceptance region in the (ν, Q^2) plane, we define its *hadron-hadron-equivalent phase space* as its image in the (p_T, y_1) under Eqs. (20). The reason for this definition is that for both hadronic and DIS collisions we can identify the parton f_1 of Fig. 3 with the "observed" parton in hadronic and DIS collisions, i.e., the parton which fragments into the observed hadron. Then the variables p_T and y_1 fully characterise the observed parton. An analogous definition holds when using x_B instead of ν as independent variable. As an example, the HERMES DIS phase space in the (ν, Q^2) plane is determined by the values of W^2_{min}, Q^2_{min} and y_{max}:

$$\begin{aligned} &\frac{Q^2_{min} + W^2_{min} - M^2}{2M} \leq \nu \leq y_{max} E_{trf} \\ &Q^2_{min} \leq Q^2 \leq M^2 + 2M\nu - W^2_{min} \,. \end{aligned} \tag{22}$$

Additionally, one may impose stronger cuts on ν, e.g., $\nu \geq \nu_{min}$, as at the EMC experiment, and in some HERMES analysis.

With Eqs. (20) it is easy to plot the hadron-hadron-equivalent DIS phase space in the (y_1, p_T) plane. As an example, we can consider the RHIC-equivalent phase space of the HERMES and EMC experiments, using $\sqrt{s_{\rm NN}} = 200$ GeV, shown in Fig. 5 left. Note that according to Eq. (21), the hadron-hadron-equivalent phase space at other center of mass energies can be obtained by a shift $y_1 \to y_1 + \Delta y_1$, see Table 4. We assume the pQCD formulae used to define the hadron-hadron-equivalent phase space to be valid at RHIC top energy for $p > p_0 = 1$ GeV: the corresponding

pQCD confidence region is plotted as a dotted line, see Eq. (24) below for details. We can see that the HERMES experiment, with $E_{trf} = 12$ and 27.6 GeV, covers less than one third of the available RHIC p_T range at $y_1 \approx -3$, with shrinking p_T coverage at larger rapidity. In the SPS/FNAL midrapidity region it reaches $p_T = 2.5$ GeV at most. Since

$$y_1 \leq \log\Big(\frac{\sqrt{s}}{2ME_{trf}}\frac{p_T}{y_{max}}\Big) \tag{23}$$

and y_{max} cannot be increased above 1, the only way to effectively reach larger values of y_1 is to increase the electron beam energy E_{trf}. Indeed, the EMC experiment, with $E_{trf} = 100 - 280$ GeV, covers a larger span in rapidity and extends to $y_1 \gtrsim 0$. Moreover, the increased energy allows one in principle to reach much higher p_T than at HERMES. However, only the $p_T \lesssim 3$ GeV region has been explored. As also shown in Fig. 5 left, the proposed Electron-Ion Collider (EIC) [40, 41] will be able to effectively study the $y_1 > 0$ region, and cover most of the RHIC phase space. Likewise, it will cover only the $y_1 < 0$ part of the LHC phase space.

When discussing hadronic collisions in the framework of collinear factorisation in pQCD, we should first define the region of validity of perturbative computations: $p_T \geq p_0$. Typically one needs $p_0 \gtrsim 1$ GeV, which agrees with the phenomenological analysis of Refs. [42, 43]. Then, the hadron-hadron phase space at a given y_1 is defined by the kinematic bounds on 2→2 parton scatterings [42]:

$$\begin{aligned}
&|y_1| \leq \cosh^{-1}\Big(\frac{\sqrt{s}}{2p_0}\Big)\\
&p_0 \leq p_T \leq \frac{\sqrt{s}}{2\cosh(y_1)}\\
&-\log\Big(\frac{\sqrt{s}}{p_T} - e^{-y_1}\Big) \leq y_2 \leq \log\Big(\frac{\sqrt{s}}{p_T} - e^{y_1}\Big)\\
&\frac{m_{hT}}{\sqrt{s}}e^{y_h}\Big(1 + \frac{p_{hT}^2}{m_{hT}^2 e^{y_h}}\Big) \leq z \leq 1
\end{aligned} \tag{24}$$

Introduction of intrinsic parton transverse momentum in the formalism, or use of next-to-leading order kinematics [44], would relax somewhat these bounds. At large rapidity, where the 2→2 phase space is becoming more and more restricted, 2→1 parton fusion processes may become the dominant mechanism, because they are sensitive to much lower fractional momenta x_i [45]. Hence, at the boundary of the hadron-hadron phase space, the presented analysis becomes unreliable.

The *DIS-equivalent hadron-hadron phase space* is defined as the image of Eqs. (24) in the (ν, Q^2, y, z_h) space under Eqs. (19). It is 4-dimensional and difficult to directly visualise. A way around this problem is to define suitable trajectories in hadron-hadron phase space averaged over y_2, and to project them into the DIS-equivalent (ν,Q^2) and (ν,z_h) phase spaces. We can define a p_{hT}- and y_h-dependent average observable as follows

$$\langle O\rangle_{p_{hT},y_h} = \frac{\int dz\, dy_1\, dy_2\, O(p_T, y_1, y_2, z)\frac{d\hat{\sigma}^{AB\to hX}}{dp_T^2 dy_1 dy_2 dz}}{\int dz\, dy_1\, dy_2 \frac{d\hat{\sigma}^{AB\to hX}}{dp_T^2 dy_1 dy_2 dz}}\,, \tag{25}$$

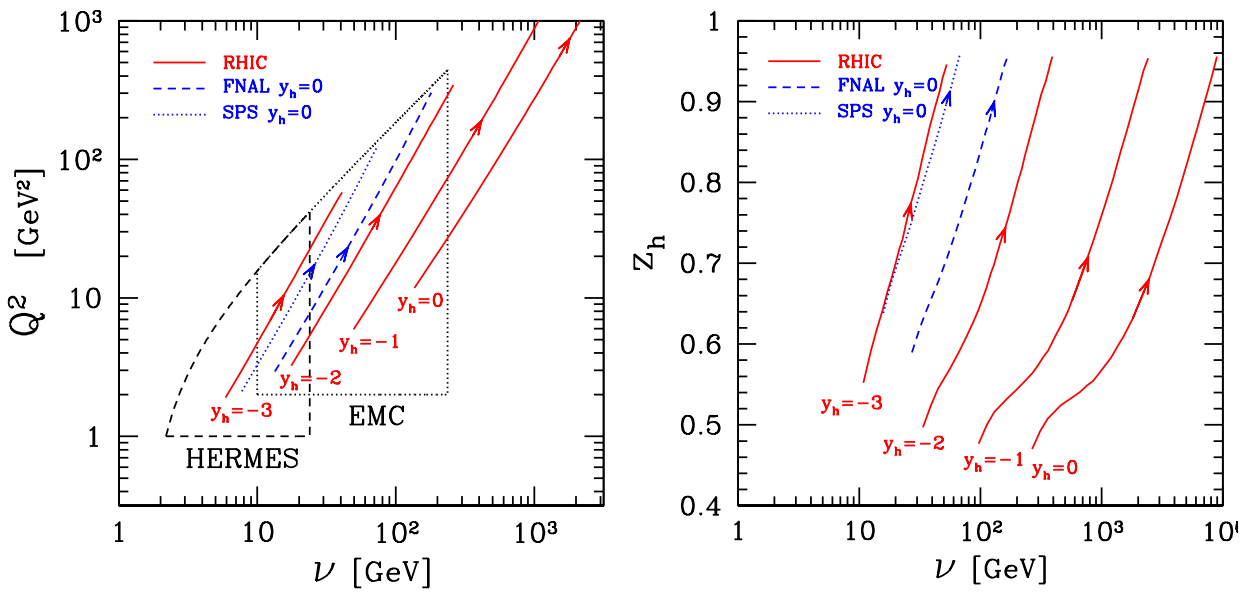

Figure 6: *left:* Fixed-y_1 hadron-hadron trajectories plotted in the DIS-equivalent (ν, Q^2) phase space for RHIC at $\sqrt{s_{\rm NN}}$ = 200 GeV and various rapidities, for FNAL and SPS at midrapidity. The dashed line encloses the HERMES phase space; the dotted line encloses the EMC phase space. The arrow indicates the direction of increasing $\langle p_T \rangle$ and $\langle z_h \rangle$. *Right:* Trajectories in the (ν, z_h) plane. The arrows indicate increasing p_T and Q^2.

where

$$\frac{d\hat{\sigma}^{AB\to hX}}{dp_T^2 dy_1 dy_2 dz} = \sum_{f_1} \frac{1}{z^2} D^h_{f_1}(z) \frac{d\hat{\sigma}^{AB\to f_1 X}}{dp_T^2 dy_1 dy_2} \,, \tag{26}$$

$d\hat{\sigma}^{AB\to f_1 X}$ is the LO pQCD differential cross-section for production of a f_1 parton in a collision of hadrons A and B (nucleons or nuclei), and $D^h_{f_1}$ is its fragmentation function into the observed hadron. Then we can define fixed-y_h trajectories $\{(\langle \nu \rangle_{p_T,\bar{y}}, \langle Q^2 \rangle_{p_T,\bar{y}}); p_T \geq p_0\}$ and $\{(\langle \nu \rangle_{p_T,\bar{y}}, \langle z_h \rangle_{p_T,\bar{y}}); p_T \geq p_0\}$ in the DIS-equivalent phase space.

As an example, in Fig. 6 we considered hadronic collisions at RHIC top energy $\sqrt{s_{\rm NN}}$ = 200 GeV and at fixed-target energies $\sqrt{s_{\rm NN}}$ = 17 − 27 GeV, and plotted the fixed-y_h trajectories in the DIS-equivalent phase space. The range of p_T spanned along each trajectory is tabulated in Table 5. The spanned range in Q^2 is limited by the maximum p_T at each rapidity, according to Eq. (24). As expected, the smaller the rapidity $y_h \approx y_1$ the smaller the spanned ν. RHIC trajectories with $y_h \lesssim -2$ span relatively low values of $\nu \lesssim 60$ GeV and large values of $z_h \gtrsim 0.5$, where the EMC and HERMES experiments have shown non negligible cold QCD matter suppression of hadron production. At higher rapidity, the larger spanned values of ν will make cold QCD matter effects less prominent.

	SPS $\sqrt{s_{\rm NN}}$ = 17.5 GeV	FNAL $\sqrt{s_{\rm NN}}$ = 27.4 GeV	RHIC $\sqrt{s_{\rm NN}}$ = 200 GeV			
y_h	0	0	0	-1	-2	-3
p_{hT}	1–8	1–12	1–90	1–60	1–25	1–9

Table 5: Range of average $\langle p_T \rangle$ spanned along trajectories at fixed rapidity y_1 at RHIC top energy $\sqrt{s_{\rm NN}}$ = 200 GeV and at fixed-target energies $\sqrt{s_{\rm NN}}$ = 17 − 27 GeV. p_{hT} is quoted in GeV.

2.3 Nuclear modification observables

In lepton-nucleus DIS, the experimental results for hadron production are usually presented in terms of the hadron multiplicity ratio R_M^h, which represents the ratio of the number of hadrons of type h produced per deep-inelastic scattering event on a nuclear target of mass A to that from a deuterium target (D). The multiplicity ratio R_M^h depends on the leptonic variables ν and Q^2, and on the hadronic variables $z = E_h/\nu$ and p_T^2 defined in Section 2.1. It is defined as the super-ratio

$$R_M^h(z, \nu, Q^2, p_T^2) = \left(\frac{N_h(z, \nu, Q^2, p_T^2)}{N_e(\nu, Q^2)}\right)_A \Bigg/ \left(\frac{N_h(z, \nu, Q^2, p_T^2)}{N_e(\nu, Q^2)}\right)_D , \tag{27}$$

where N_h is the yield of semi-inclusive hadrons in a given (z, ν, Q^2, p_T^2)-bin, and N_e the yield of inclusive deep-inelastic scattering leptons in the same (ν,Q^2)-bin. Normalizing the hadron yield to the DIS yield allows one to cancel, to a large extent, initial-state nuclear effects such as (anti)shadowing of PDFs and isolates final-state nuclear modifications of hadron production as a deviation of R_M from 1. A suppression of R_M is experimentally observed to increase with z, and to decrease with ν, and more mildly with Q^2. When plotting R_M as a function of p_T, one observes a suppression at small p_T and an enhancement above $p_T \approx 1.5$ GeV. This behaviour is also known as "Cronin effect". The amount of transverse momentum broadening (defined with respect to the direction of the virtual photon, see Fig. 4) is quantified via

$$\Delta\langle p_T^2\rangle^h = \langle p_T^2\rangle_A^h - \langle p_T^2\rangle_D^h . \tag{28}$$

Here, $\langle p_T^2\rangle_A^h$ is the average transverse momentum squared of a hadron of type h produced on a nuclear target A

$$\langle p_T^2\rangle^h = \frac{\sum_{p_T,z,\nu,Q^2} p_T^2\, N_h(z, \nu, Q^2, p_T^2)|_A}{\sum_{p_T,z,\nu,Q^2} N_h(z, \nu, Q^2, p_T^2)|_A} , \tag{29}$$

and $\langle p_T^2\rangle_D^h$ is the same quantity for a Deuterium target. The hadron p_T-broadening is supposed to be accumulated mainly by elastic scatterings of its parent parton on its way through the nucleus, hence to be a sensitive probe of the quark lifetime.

In high energy heavy-ion collisions what is usually presented is the ratio of the hadron transverse momentum spectrum measured in $A + A$ at a given rapidity y and impact parameter b (or centrality class) normalised by the nuclear overlap function $T_{AB}(b)$ – related to the "parton luminosity" at a given b – over the $p + p$ spectrum:

$$R_{AB}^h(p_T, y; b) = \frac{1}{T_{AB}(b)} \frac{d^2N_h^{A+B}(b)}{dp_T^2 dy} \Bigg/ \frac{d^2\sigma_h^{p+p}}{dp_T^2 dy} . \tag{30}$$

In the absence of nuclear effects, one would expect $R_{AB} = 1$.

Medium modifications of hadron production in nDIS and heavy-ion collisions can also be revealed by means of multi-particle azimuthal correlations, which are sensitive to the underlying parton-medium interaction and to the properties of the medium. For example, two-hadron correlations measured at RHIC revealed significant broadening and softening of associated hadrons on the away side of a triggered high-p_T particle, which is consistent with the observation of the hadron suppression in the single inclusive measurements. In nDIS processes, the distribution of associated sub-leading hadrons to the leading hadron is challenging accepted theoretical models of single inclusive hadron suppression.

3 Space-time evolution of hadronisation

Even though hadronisation is a non perturbative process, a few features can be extracted from general grounds. A parton created in an high-energy collision can travel in the vacuum as a free particle only for a limited time because of colour confinement: it has to dress-up in a colour-field of loosely bound partons, which eventually will evolve into the observed hadron wave function. The same dressing process can be expected for partons traveling in QCD matter, but will be modified by interactions with the surrounding medium. In a deconfined nuclear medium such as the QGP, the dressing process might furthermore be delayed until the medium cools down and comes closer to the confinement phase transition.

The bare parton-medium cross section is dominated by the elastic $a + b \to a + b$ parton-parton scattering and gluon bremsstrahlung, of order $\mathcal{O}(10)$ mb. However, the dressed parton is likely to develop an inelastic cross section of the order of the hadronic one ($\mathcal{O}(40)$ mb.), becoming subject to nuclear absorption similarly to the final state hadron. Hence, it can be considered a "prehadron" and denoted by h_*. The prehadron may still be in a coloured state and radiate gluons but is likely to neutralise its colour before its wave function collapses on the observed hadron's wave function. We can therefore identify 3 relevant time scales, see Fig. 7: (1) the "prehadron production time" or "quark lifetime" t_{preh}, at which the dressed quark develops an inelastic cross section, (2) the "colour neutralisation time" t_{cn}, at which gluon bremsstrahlung stops, and (3) the "hadron formation time" t_h, at which the final hadron is formed. Typically, model applications further simplify the process and assume $t_{preh} = t_{cn}$. We would like to remark that the prehadron and the formation times are introduced as a phenomenological tool, rather than a well defined theoretical construct, in order to distinguish the stage in which the parton can be described as an asymptotically free particle and treated in pQCD from the stage in which colour confinement and non perturbative

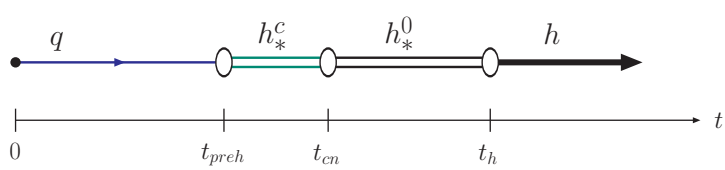

Figure 7: Sketch of the time evolution of the hadronisation process with definition of the relevant time scales. A quark q created at time 0 in a hard collision turns into a coloured prehadron h_*^c, which subsequently neutralises its colour, h_*^0, and collapses on the wave function of the observed hadron h. Gluon radiation lasts until colour neutralisation.

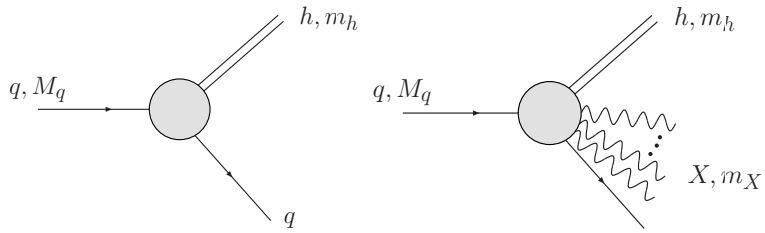

Figure 8: Quark hadronisation by emission of one parton (*left*) and emission of one parton accompanied by many soft gluons (*right*).

interactions kick in and warrant a treatment in terms of different degrees of freedom. Such a phenomenology is well suited to the present status of the theoretical and experimental investigation, but will need to be substantiated or replaced by a more fundamental QCD description. Finally, note that strictly speaking the very question "Is the prehadron formed within or without the medium?" is ill-posed: in quantum mechanics it can happen one way in the amplitude and the other in its complex conjugate, and the interference between the two may be non-negligible [46].

A simple estimate of the hadron formation time $\langle t_h \rangle$ can be obtained by defining it as the time for the struck partons to build up its colour field and to develop the hadronic wave function [47]. In the hadron rest frame this time is related to the hadron radius R_h, and in the laboratory frame it is boosted to:

$$\langle t_h \rangle \propto R_h \frac{E_h}{m_h} = R_h \frac{z\nu}{m_h} \tag{31}$$

In Table 6 we show the hadron formation time estimated by Eq. (31) for a typical 7 GeV pion ($R_h \approx 0.67$ fm) at HERMES and RHIC. We have $\langle t_\pi \rangle \approx 40$ fm $\gg R_A$, which points towards a long quark lifetime with hadron formation outside the medium. However, for kaons and protons ($R_h \approx 0.58$ fm and 0.86 fm) we obtain much shorter formations times $\langle t_K \rangle \approx 10$ fm and $\langle t_p \rangle \approx 8$ fm, which are comparable to the size of the medium.

A more detailed estimate [25] can be obtained by looking at hadronisation in light-cone coordinates, where for any 4-vector a^μ, we write $a^\mu = (a^+, a^-, \vec{a}_T)$ with $a^\pm = (a^0 \pm a^3)/\sqrt{2}$ and $\vec{a}_T = (a^1, a^2)$. We consider a relativistic on-shell quark of mass M_q and plus-momentum p^+, hadronizing into a hadron of mass m_h and 4 momentum $p_h^+ = zp^+$. Minimally, hadronisation proceeds by emission of an additional, typically light, parton to carry away the extra colour, see Fig. 8 left. The process in momentum space is

$$\left[p^+, \frac{M_q^2}{2p^+}, \vec{0}_T\right] \longrightarrow \left[zp^+, \frac{m_h^2 + \vec{k}^2}{2zp^+}, \vec{k}\right] + \left[(1-z)p^+, \frac{\vec{k}^2}{2(1-z)p^+}, -\vec{k}\right] \tag{32}$$

where we imposed 4-momentum conservation. In time-ordered perturbation theory, the light-cone separation Δy^+ between the initial and final state can be estimated by the uncertainty principle:

$$\Delta y^+ \approx 1/\Delta p^- = \frac{2z\,(1-z)\,p^+}{\vec{k}^2 \;+\; (1-z)\,m_h^2 - z\,(1-z)\,M_q^2}\,, \tag{33}$$

where $\Delta p^- = p^-_{q'} + p^-_h - p^-_q$. The hadron formation time is then

$$\langle t_h \rangle \approx \sqrt{2}\,\Delta y^+\,. \tag{34}$$

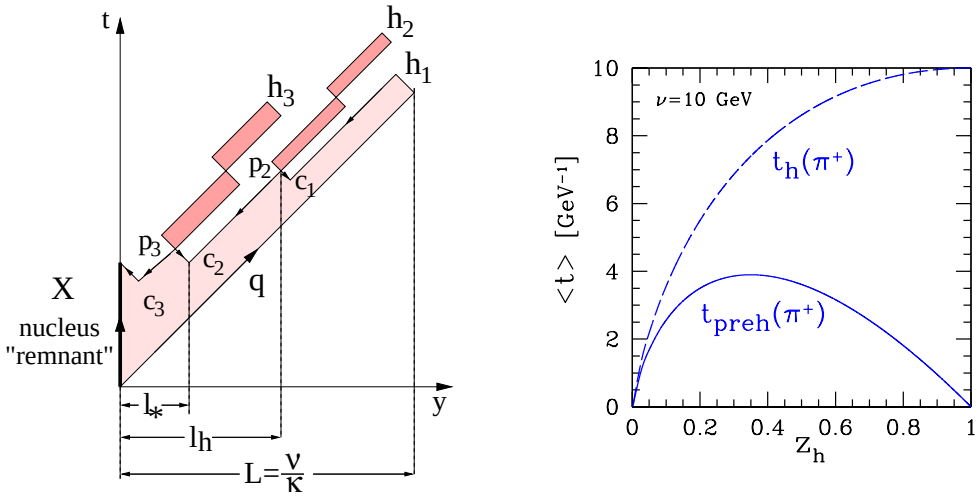

Figure 9: *Left*: Hadronisation in the Lund string model in the target rest frame. *Right*: Prehadron production time ($\langle t_{preh}\rangle$) and hadron formation times ($\langle t_h\rangle$) for $\nu = 10$ GeV quarks fragmenting into pions, as computed in the Lund string model [48].

This estimate should actually be considered an upper limit. Indeed, hadronisation is a non-perturbative process, hence it will be accompanied by the emission of many soft gluons, see Fig. 8 right. The system of emitted parton plus soft-gluons has an invariant mass m_X^2. Taking this into account, we should add an additional zm_X^2 term at the denominator of Eq. (32), which would reduce the formation time. In Table 6 we show the hadron formation time estimated by Eq. (33) for typical hadrons at HERMES ($z \approx z_h \approx 0.5$, $p^+/\sqrt{2} \approx \nu \approx 14$ GeV) and typical mid-rapidity hadrons at RHIC ($z \approx 0.7$, $zp^+ \approx p_T^h \approx 7$ GeV), where we assumed $\vec{k}^2 \approx \Lambda_{QCD}^2$. As in the previous estimate, high-p_T pions are formed outside the medium ($\langle t_\pi\rangle \approx 30$ fm), kaons ($\langle t_k\rangle \approx 10$ fm) and protons ($\langle t_p\rangle \approx 4$ fm) have formation times comparable to the medium size, and heavy mesons are produced rapidly inside the medium.

At least for light quarks and gluons, these estimates can be used to justify the computation of hadron quenching in terms of parton-medium interactions alone, as done in radiative energy loss models [49–51]. However, even if the hadron is fully formed outside the nucleus, the colour field which the quark is building up might start interacting with the medium much earlier. In other words, the quark lifetime might actually be smaller than in the above estimates due to the formation of a prehadron, whose production time we are going to estimate.

A successful non perturbative model of hadronisation is the Lund string model [52], see Fig. 9 left. The confined colour field stretching from the struck quark to the rest of the nucleus is modeled as a string of tension $\kappa_{str} \approx 1$ GeV/fm, and spans the lightly shaded area in space-time. The prehadron formation point is identified with the $q\bar{q}$ pair production point C_i which breaks the string in smaller pieces [53]. Hadrons are formed at points P_i when a quark and an antiquark at the endpoint of a string fragment meet. The subscript i indicates the so-called rank of the produced (pre)hadron, counted from the right of the figure. Average prehadron production times can be

Estimate	kinematics	π	K	p	D	B
Eq. (31)	HERMES	34 fm	8 fm	6 fm		
Eq. (31)	RHIC	48 fm	12 fm	9 fm		
Eq. (34)	HERMES	36 fm	11 fm	4 fm	1 fm	0.2 fm
Eq. (34)	RHIC	26 fm	10 fm	4 fm	1 fm	0.2 fm
Eq. (35)	HERMES	13 fm	8 fm	25 fm		
Eq. (35)	RHIC	7 fm	5 fm	14 fm		

Table 6: Estimates of typical hadron formation times $\langle t_h \rangle$ for pions, kaons, protons, and D and B mesons at HERMES ($z_h \approx 0.5$, $\nu \approx 14$ GeV) and at RHIC at mid-rapidity ($p_T^h \approx 7$ GeV/c) obtained with Eqs. (31), (34), and (35).

analytically computed [48, 53, 54] and have the following general structure:

$$\langle t_{preh} \rangle = f(z_h)\,(1 - z_h)\,\frac{z_h \nu}{\kappa_{str}} \quad , \quad \langle t_h \rangle = \langle t_{preh} \rangle \; + \; \frac{z_h \nu}{\kappa_{str}} \, , \tag{35}$$

where ν is the struck quark energy. The factor $z_h \nu$ can be understood as a Lorentz boost factor. The $(1 - z_h)$ factor is due to energy conservation: a high-z_h hadron carries away an energy $z_h \nu$; the string remainder has a small energy $\epsilon = (1 - z_h)\nu$ and cannot stretch farther than $L = \epsilon/\kappa_{str}$. Thus the string breaking must occur on a time-scale proportional to $1 - z_h$. The function $f(z_h)$ is a small correction of $\langle t_{preh} \rangle$, which can be computed analytically in the standard Lund model [48, 53], and $\kappa_{str} = (1 \text{ GeV/fm})\; r_\pi^2 / r_h^2$, with r_h the hadron radius, are taken from Ref. [48] The resulting pion formation time scaled by a factor ν/κ_{str} is plotted in Fig. 9 left. A typical pion produced at HERMES energies (i.e. with fractional energy $z_h \approx 0.5$ from a parent quark with energy $\nu \approx 14$ GeV) has $\langle t_{preh} \rangle \approx 6$ fm $\lesssim R_A$ and $\langle t_h \rangle \approx 13$ fm $\gtrsim R_A$, with similar values at RHIC at mid-rapidity. The final hadron is typically formed at the periphery or outside the nucleus so that its interaction with the medium is negligible (see Table 6). However, the prehadron is formed inside and can start interacting with the nucleus. A detailed space-time analysis of hadronisation in the PYTHIA/JETSET Monte Carlo implementation of the Lund string model has been performed in [55], with similar conclusions regarding the magnitude of the pion prehadron production time.

In Ref. [56, 58, 59] the formation of a leading hadron ($z_h \gtrsim 0.5$) is described in a pQCD model, see Fig. 10. The struck quark radiates a gluon. The gluon then splits into a $q\bar{q}$ pair, and the $\bar{q}$ recombines with the struck q to form the leading prehadron, which later on collapses on the hadron wave function. The cross-section can be computed from the modulus squared of the sum of the two gauge-invariant amplitudes shown in the figure. At $z_h \approx 1$, higher twist effects spoil this

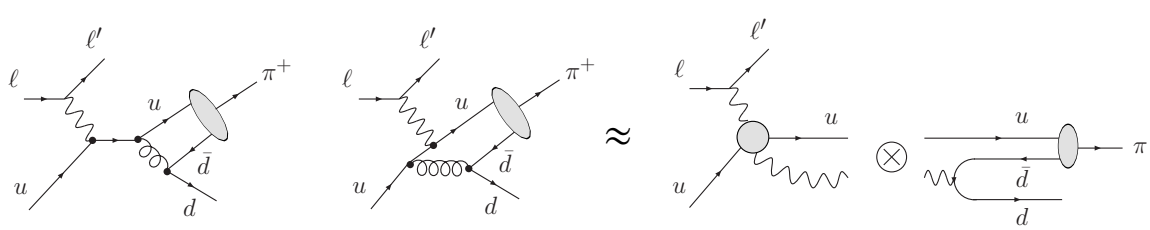

Figure 10: Diagrams for leading hadron formation in $\ell + A$ collisions: Gauge-invariant set [56] (*left*), and dipole-model approximation [57] (*right*).

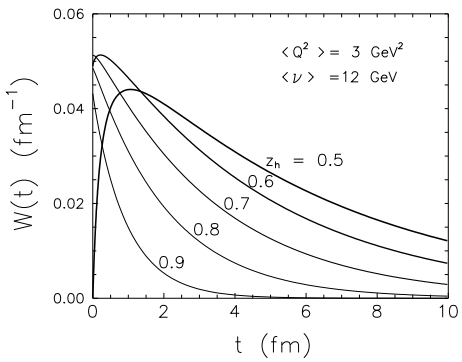

Figure 11: Probability distribution of the prehadron production time $t_{preh} \equiv t$ obtained in the colour-dipole model of [57].

simple mechanism for hadronisation. The dipole model of Ref. [57] approximates the described cross-section as a convolution of a Gunion-Bertsch radiation cross section [60] with the gluon splitting plus quark recombination process, see Fig. 10 right. The prehadron is identified with the $q\bar{q}$ pair which includes the struck quark, and its production time is identified with the time at which the gluon becomes decoherent from the struck quark. (We should note that, strictly speaking, at the production time the struck quark-gluon system is in an octet state until gluon splitting occurs; however, in this model, gluon radiation is neglected during the octet stage). The model can compute the probability distribution in the prehadron production time, see Fig. 11, and the average $\langle t_{preh} \rangle$ is

$$\langle t_{preh} \rangle \propto (1 - z_h) \frac{z_h \nu}{Q^2} \ . \tag{36}$$

The interpretation of the $1-z_h$ factor is in terms of energy conservation: the longer the struck quark propagates, the larger its energy loss; hence to leave most of its energy to a $z_h \to 1$ hadron, the quark must be short lived. The scale is set by $\kappa_{dip} = Q^2$. At HERMES, with $Q^2 \approx 10$ GeV/fm, one obtains for pion production $\langle t_{preh} \rangle \lesssim 5$ fm at $z_h > 0.5$: pre-pions are formed inside the medium. At RHIC, where $Q^2 \propto p_T^2$, and $z_h \nu \approx p_T$ for mid-rapidity hadrons, one obtains the counter-intuitive result that $\langle t_{prep} \rangle \propto 1/p_T$: prehadrons are formed the quicker the higher their transverse momentum [57, 61], typically inside the medium.

In summary, there are considerable uncertainties in the theoretical estimates of the formation and production time, hence of the length of the partonic phase of the hadronisation process. It is of foremost importance to establish the scale of $\langle t_{preh} \rangle$ and its dependence on the kinematic variables of the scattering process, through a careful analysis of experimental data and tests of phenomenological models. It will be the first step into a deeper and more detailed understanding of the space-time evolution of the hadronisation process.

4 Short review of fixed target experiments

Short review of EMC, HERMES results; CLAS preliminary. Theoretical results discussed throughout; open questions.

	MANUEL		s-eRHIC		eRHIC		ELIC		LHeC	
	Ca	e	Au	e	Au	e	Ca	e	Pb	e
E [GeV/A or GeV]	7.5	3	**100**	**2**	**100**	**20**	**75**	**7**	2750	70
L_{peak} [10^{33} cm^{-2}s^{-1}]	1		**0.1**		**1**		**100**		1.0	

Table 7: Energies, E, and peak luminosities, L_{peak}, for $e + A$ collisions at the EIC (staged-eRHIC, eRHIC, and ELIC designs), and at the LHeC (Ring-Ring mode). In bold face are the parameters used for the simulations presented in this document.

5 EIC capabilities

An electron-ion collider would significantly complement and add new dimensions to the experimental studies at fixed target facilities, by extending the range of accessible lepton, E_e, and ion, E_A, energies. Proposed designs for an electron-ion collider currently have a fairly wide range of luminosities and center of mass energies, see Table 7. The Electron-Ion Collider (EIC) is a proposed US based facility, which will provide $E_e = 3 - 20$ GeV and $E_A = 15 - 100$ GeV/A [40, 41]. There are currently 2 complementary concepts to realize it [41]: (i) eRHIC will add an electron beam to the existing RHIC ion accelerator at BNL - the option of staging it, and first realize a lower energy version with $E_e = 2 - 4$ GeV, based on an energy recovery linear accelerator for the electron beam is being actively discussed [62, 63]; (ii) ELIC will add an ion accelerator to the CEBAF upgraded 12 GeV electron ring at Jefferson Lab. The eRHIC concept emphasizes the energy range; the ELIC concept will reach up to 100 times more luminosity, but with lower maximum energy. The Large Hadron-electron Collider (LHeC) is a proposed upgrade of the LHC at CERN [64], and will reach much higher energies than the EIC, still with a good luminosity. Because of the very large energy asymmetry of the lepton and hadron beams, it is not yet clear if it will be possible to design an optimized detector for both $e + p$ and $e + A$ collisions. Finally, the idea of building a low-energy electron-ion, collider at FAIR has recently been advanced [65]: the goal of the "Mainz concept for a Nucleon electron collider at FAIR" (MANUEL@FAIR) is to have a center of mass energy between HERMES and COMPASS, but up to a factor 100 higher luminosity. Here, we will focus on the EIC capabilities, but most of the discussed measurements will be in principle possible at MANUEL and the LHeC, as well.

The EIC will provide virtual photons with energies in the $\nu = 10 - 1600$ GeV range, large Q^2 up to 1000 GeV^2, and low $x \gtrsim 10^{-5}$; the collider mode will allow one to separate current from target fragmentation; its high luminosity will allow access to rare signals, multi-differential measurements, and dihadron or γ-hadron correlations. At EIC we will be able to cross-check HERMES and CLAS measurements, while having many more channels at our disposal and an extended kinematic range for studying hadronisation inside the nucleus at low-ν, and at high-ν testing basic QCD processes at the parton level, such as non-abelian parton energy loss and the space-time evolution of the DGLAP shower. EIC will be unique, compared to HERA (HERMES) and JLab (CLAS), in the following areas:

- At the large ν accessible at the EIC, hadrons will clearly be formed outside the nuclear medium, so that effects due to the propagation of the struck quark can be experimentally isolated. One will have new access to p_T-broadening studies, which can cleanly probe the parton radiative energy loss as predicted by pQCD at asymptotic energy. It will also be pos-

sible to study in detail the interplay of radiative and collisional parton energy loss, medium modifications of the DGLAP evolution, and test factorisation for the fragmentation functions.

- Heavier mesons like η and ϕ will be more abundantly produced than at HERMES/JLab. At both medium-low and large ν, comparing their quenching to that of their lighter π and K counterparts will provide important clues about parton propagation and hadronisation.

- The EIC excellent low-x coverage provides increased production of heavy flavor and quarkonia. In particular, it will be possible to study the heavy quarks energy loss through the B and D meson suppression. Theoretical mechanisms proposed to explain J/ψ suppression in $p+A$ and $A+A$ collisions can be put to the test in a clean experimental environment by studying J/ψ, ψ' and χ spectra.

- The large Q^2 coverage will access the true perturbative QCD regime, whose prediction can be more confidently tested against the data, in particular colour transparency effects and the Q^2-dependence of the observables discussed in this review, like the hadron p_T-broadening.

- Baryon production through parton fragmentation will also be accessible, because of the collider mode and the accessible final-state invariant masses. This will allow studying baryon transport in cold QCD matter and the baryon anomaly observed in fixed target $e+A$ collisions at HERMES and in heavy-ion collisions RHIC. The ability to identify a good variety of baryons, including the strange and charmed sector, will be a key to this program.

- For the first time, jet physics in DIS with a nuclear target will be experimentally accessible. In particular, medium modifications of the jet shape, and the comparison of light-quark to heavy-quark and gluon initiated jets will shed light on the mechanisms underlying parton energy loss. These studies can also be extended to dijet or γ-jet correlations.

In summary, the collider kinematics and associated detectors with excellent calorimetry, hadron detection, and rapidity coverage, will allow for a comprehensive program to better understand how energy loss and hadronisation occur in cold QCD matter.

6 Simulations

6.1 Method

The Monte Carlo generator used in the simulation is PYTHIA 6.4.19. Although this generator only simulates electron scattering on nucleons and does not include nuclear effects such as Fermi motion, it is sufficient for our purpose to study the kinematical coverages and to extract rates for the multiplicity ratios. For the present study, we have generated 10^6 events per collider and per target (p,n). To select DIS events, the following cuts on Q^2 and W are applied: $Q^2 > 1$ GeV^2 and $W > 2$ GeV for staged eRHIC, and $Q^2 > 1.5$ GeV^2 and $W > 4$ GeV for eRHIC and ELIC.

Table 8 summarizes the generated cross section of subprocesses for each design. About 80 % of the generated events are DIS. Table 9 shows multiplicities for several particle types on deuterium. Pions and kaons are produced copiously. Therefore, strange quark hadronization can be

Subprocess	σ for eRHIC (mb)	σ for s-eRHIC (mb)	σ for ELIC (mb)
All included subprocesses	3.231D-04	2.047D-04	2.224D-04
f + f' − > f + f' (QCD)	2.148D-05	2.545D-05	2.723D-05
f + fbar − > f' + fbar'	3.811D-08	0	0
f + fbar − > g + g	4.557D-08	0	0
f + g − > f + g	1.666D-05	4.688D-06	5.197D-06
g + g − > f + fbar	1.025D-07	0	0
g + g − > g + g	9.926D-06	2.623D-06	2.669D-06
q + gamma* − > q	2.515D-04	1.636D-04	1.771D-04
f + gamma*_T − > f + g	6.453D-06	3.186D-06	3.670D-06
f + gamma*_L − > f + g	3.686D-07	1.940D-07	2.232D-07
g + gamma*_T − > f + fbar	1.319D-05	3.880D-06	4.902D-06
g + gamma*_L − > f + fbar	3.411D-06	1.167D-06	1.409D-06
VMD * hadron	4.825D-05	3.277D-05	3.510D-05
direct * hadron	2.343D-05	8.425D-06	1.020D-05
DIS * hadron	2.515D-04	1.636D-04	1.771D-04

Table 8: Cross section per nucleon of subprocesses produced by Pythia for different collider configurations.

studied with high precision. In the heavy flavor sector, a decent number of *D* mesons is produced. However, dedicated studies of their reconstruction channels have to be performed in order to optimize the difficulty of reconstructing the decay products versus the statistical precision. The same issue exists for B meson and J/ψ in addition to the fact that their production cross section is much smaller. Taking the example of D^0 mesons, their production cross section is five time larger et eRHIC that ELIC due to the higher center of mass energy. However, this deficit get reversed to the advantage of ELIC due to the two order of magnitude more luminosity. Moreover, the tracking capability of the detector, its particle identification and vertex reconstruction will play a crucial role in the success of the program.

6.2 Detection

Since we do not have yet a detailed enough detector concept to simulate its acceptance, we apply a simple geometrical cut retaining only particles with a polar angle between 3 and 177 degrees to exclude the beam pipes. This is good for a first rough estimation of the detector acceptance. However, we note that the angular coverage is very important for heavy particles, especially baryons, that are produced very close to the direction of the beam nuclei. On the contrary, with DIS cuts there is no issue with electrons because of the boost coming from the nuclei, electrons are in the acceptance. However, the successful reconstruction of heavy mesons (B, D, J/Ψ4...) needs excellent vertex determination ($\sim 100\mu m$).

Hadron	Detection channel	eRHIC	s-eRHIC	ELIC
π^0	$\gamma\gamma$	3885	3060	3174
π^+	direct	3411	2683	2781
π^-	direct	3505	2770	2869
ρ^0	$\pi^+\pi^-$	620	489	507
ρ^+	$\pi^+\pi^0$	583	461	527
ρ^-	$\pi^0\pi^-$	584	460	474
η	$\gamma\gamma$	413	323	339
ω	$\pi^+\pi^-\pi^0$	575	457	472
η'	$\pi^+\pi^-\eta$	112	86	89
ϕ	K^+K^-	47	34	35
K^+	direct	401	306	320
K^-	direct	336	243	256
K^0_s	$\pi^+\pi^-$	352	260	273
p	direct	714	651	659
$\bar{p}$	direct	181	125	133
n	direct	635	587	595
$\bar{n}$	direct	166	113	120
Λ	$p\pi^-$	145	125	128
Σ^+	$p\pi^0$	20	16	17
Σ^0	$\Lambda\gamma$	21	18	18
D^0	n/a	31	18	20
D^+	n/a	10	6	6
B^0	n/a	0.2	0.06	0.08
B^+	n/a	0.3	0.04	0.1
J/Ψ	n/a	0.02	0.002	0.007

Table 9: Simulation of multiplicity from Pythia with cuts on Q^2 and W: $Q^2 > 1.5$ GeV^2 and W > 4 GeV for 1000 events on deuterium.

6.3 Results

Figure 12 shows the correlation between Q^2 and x_B for the three EIC designs. In this plot we take into account the luminosity by using a threshold on the number of accepted events. The comparison between eRHIC and ELIC shows a better coverage at high Q^2 for ELIC and at low x_B for eRHIC. This is due to the long tail of the Q^2 distribution enhanced by the great luminosity. On the contrary, the x_B distribution decreases faster since it depends only on the available center of mass energy.

Figure 13 shows projected statistical errors for the charged pions multiplicity ratio at the EIC (eRHIC design) with 10 weeks of beam compared to data from the HERMES experiment [19]. ELIC will benefit of a 100 times larger luminosity, therefore we can expect as much kaons in ELIC as pions in eRHIC. With both designs, the huge amount of data in both cases is extremely useful to produce multidimensional study, where HERMES gives two-dimensional plots, one could have up to 5-dimensional analysis and completely understand the dependence of the multiplicity ratios

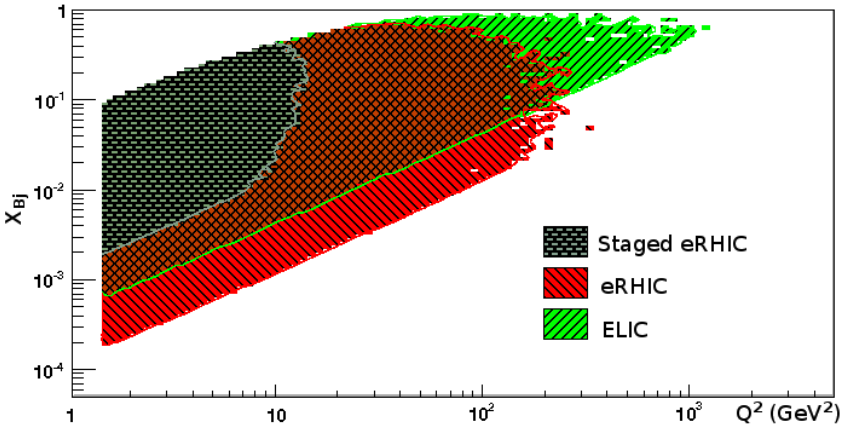

Figure 12: Kinematic coverage of the different EIC designs. This coverage take account of the luminosity given in table 7 and the cross section given by Pythia (Tables 8

on the kinematic variables.

In the future, this simulation will need to be improved by combining it with realistic detector simulation, especially to evaluate systematics errors, and by adding a simulation of nuclear effects. Some solutions have to be explored to reconstruct exotic meson and baryons to evaluate the efficiency we can achieve for those particles, which are very interesting. Detection of heavy flavor and quarkonium needs to be addressed, as well. We also plan a dedicated study for an hadronization program at the staged eRHIC.

References

[1] V. N. Gribov and L. N. Lipatov, Sov. J. Nucl. Phys. **15** (1972) 438–450.

[2] G. Altarelli and G. Parisi, Nucl. Phys. **B126** (1977) 298.

[3] Y. L. Dokshitzer, Sov. Phys. JETP **46** (1977) 641–653.

[4] B. Andersson, Camb. Monogr. Part. Phys. Nucl. Phys. Cosmol. **7** (1997) 1–471.

[5] G. Marchesini and B. R. Webber, Nucl. Phys. **B310** (1988) 461.

[6] J. D. Bjorken, Lect. Notes Phys. **56** (1976) 93.

[7] S. J. Brodsky, . Invited talk given at 3rd Lake Louise Winter Inst. on QCD: Theory and Experiment, Lake Louise, Canada, Mar 6-12, 1988.

[8] J. W. Cronin *et al.*, Phys. Rev. **D11** (1975) 3105.

[9] D. Antreasyan *et al.*, Phys. Rev. **D19** (1979) 764.

[10] J. C. Collins, D. E. Soper and G. Sterman, Adv. Ser. Direct. High Energy Phys. **5** (1988) 1–91 [hep-ph/0409313].

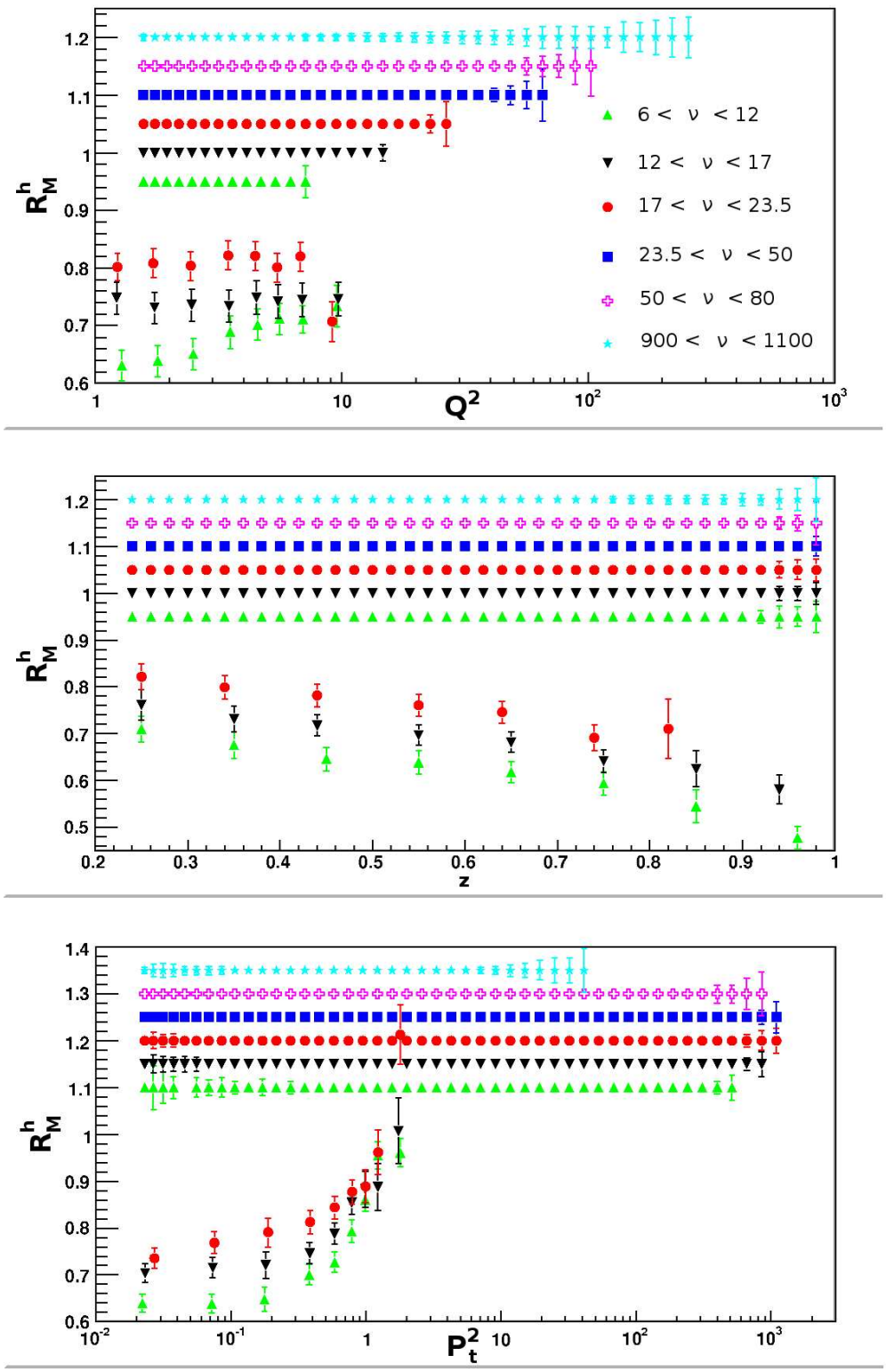

Figure 13: Comparison of charged pions multiplicity ratio on a *Xe* target at HERMES and on an isoscalar target at the EIC (eRHIC design) as a function of z, Q^2 and p_T for several cuts in ν. To simulate eRHIC, we use a quantity of data equivalent to 10 weeks of beam. Data from the HERMES experiment are taken from Ref. [19].

[11] P. M. Nadolsky *et al.*, 0802.0007.

[12] A. D. Martin, R. G. Roberts, W. J. Stirling and R. S. Thorne, Phys. Lett. **B604** (2004) 61–68 [hep-ph/0410230].

[13] G. Watt, A. D. Martin, W. J. Stirling and R. S. Thorne, 0806.4890.

[14] D. de Florian, R. Sassot and M. Stratmann, Phys. Rev. **D75** (2007) 114010 [hep-ph/0703242].

[15] S. Albino, B. A. Kniehl and G. Kramer, 0803.2768.

[16] S. Albino *et al.*, 0804.2021.

[17] **HERMES** Collaboration, A. Airapetian *et al.*, Eur. Phys. J. **C20** (2001) 479–486 [hep-ex/0012049].

[18] **HERMES** Collaboration, A. Airapetian *et al.*, Phys. Lett. **B577** (2003) 37–46 [hep-ex/0307023].

[19] **HERMES** Collaboration, A. Airapetian *et al.*, Nucl. Phys. **B780** (2007) 1–27 [0704.3270].

[20] **HERMES** Collaboration, A. Airapetian *et al.*, Phys. Rev. Lett. **96** (2006) 162301 [hep-ex/0510030].

[21] **BRAHMS** Collaboration, I. Arsene *et al.*, Nucl. Phys. **A757** (2005) 1–27 [nucl-ex/0410020].

[22] B. B. Back *et al.*, Nucl. Phys. **A757** (2005) 28–101 [nucl-ex/0410022].

[23] **STAR** Collaboration, J. Adams *et al.*, Nucl. Phys. **A757** (2005) 102–183 [nucl-ex/0501009].

[24] **PHENIX** Collaboration, K. Adcox *et al.*, Nucl. Phys. **A757** (2005) 184–283 [nucl-ex/0410003].

[25] A. Adil and I. Vitev, Phys. Lett. **B649** (2007) 139–146 [hep-ph/0611109].

[26] J. Carlson, J. B. Kogut and V. R. Pandharipande, Phys. Rev. **D28** (1983) 2807.

[27] T. Hatsuda and T. Kunihiro, Phys. Rept. **247** (1994) 221–367 [hep-ph/9401310].

[28] **MiniBooNE** Collaboration, A. A. Aguilar-Arevalo *et al.*, Phys. Rev. Lett. **100** (2008) 032301 [0706.0926].

[29] **MINOS** Collaboration, P. Adamson *et al.*, 0806.2237.

[30] S. Dytman, H. Gallagher and M. Kordosky, 0806.2119.

[31] O. Buss, T. Leitner, U. Mosel and L. Alvarez-Ruso, Phys. Rev. **C76** (2007) 035502 [0707.0232].

[32] T. Leitner, L. Alvarez-Ruso and U. Mosel, Phys. Rev. **C74** (2006) 065502 [nucl-th/0606058].

[33] T. Leitner, L. Alvarez-Ruso and U. Mosel, Phys. Rev. **C73** (2006) 065502 [nucl-th/0601103].

[34] T. Leitner, U. Mosel and L. Alvarez-Ruso, Int. J. Mod. Phys. **A22** (2007) 416–423 [nucl-th/0608037].

[35] R. D. Field, . Redwood City, USA: Addison-Wesley (1989) 366 p. (Frontiers in physics, 77).

[36] J. C. Collins and D. E. Soper, Nucl. Phys. **B193** (1981) 381.

[37] A. Accardi, Phys. Rev. **C76** (2007) 034902 [0706.3227].

[38] **HERMES** Collaboration, P. B. van der Nat, Acta Phys. Polon. **B35** (2004) 139–143.

[39] **European Muon** Collaboration, J. Ashman *et al.*, Z. Phys. **C52** (1991) 1–12.

[40] A. Deshpande, R. Milner, R. Venugopalan and W. Vogelsang, Ann. Rev. Nucl. Part. Sci. **55** (2005) 165–228 [hep-ph/0506148].

[41] **EIC** Collaboration, C. A. Aidala, 0806.4933.

[42] K. J. Eskola and H. Honkanen, Nucl. Phys. **A713** (2003) 167–187 [hep-ph/0205048].

[43] A. Accardi and M. Gyulassy, Phys. Lett. **B586** (2004) 244–253 [nucl-th/0308029].

[44] V. Guzey, M. Strikman and W. Vogelsang, Phys. Lett. **B603** (2004) 173–183 [hep-ph/0407201].

[45] A. Accardi, Acta Phys. Hung. **A22** (2005) 289–299 [nucl-th/0405046].

[46] B. Z. Kopeliovich *et al.*, 0809.4613.

[47] Y. L. Dokshitzer, V. A. Khoze, A. H. Mueller and S. I. Troian, . Gif-sur-Yvette, France: Ed. Frontieres (1991) 274 p. (Basics of).

[48] A. Accardi, D. Grunewald, V. Muccifora and H. J. Pirner, Nucl. Phys. **A761** (2005) 67–91 [hep-ph/0502072].

[49] E. Wang and X.-N. Wang, Phys. Rev. Lett. **89** (2002) 162301 [hep-ph/0202105].

[50] F. Arleo, JHEP **11** (2002) 044 [hep-ph/0210104].

[51] M. Gyulassy, P. Lévai and I. Vitev, Nucl. Phys. **B594** (2001) 371–419 [nucl-th/0006010].

[52] B. Andersson, G. Gustafson, G. Ingelman and T. Sjostrand, Phys. Rept. **97** (1983) 31–145.

[53] A. Bialas and M. Gyulassy, Nucl. Phys. **B291** (1987) 793.

[54] A. Accardi, V. Muccifora and H.-J. Pirner, Nucl. Phys. **A720** (2003) 131–156 [nucl-th/0211011].

[55] K. Gallmeister and T. Falter, Phys. Lett. **B630** (2005) 40–48 [nucl-th/0502015].

[56] E. L. Berger, Z. Phys. **C4** (1980) 289.

[57] B. Z. Kopeliovich, J. Nemchik, E. Predazzi and A. Hayashigaki, Nucl. Phys. **A740** (2004) 211–245 [hep-ph/0311220].

[58] E. L. Berger, Phys. Lett. **B89** (1980) 241.

[59] B. Z. Kopeliovich, H. J. Pirner, I. K. Potashnikova and I. Schmidt, Phys. Lett. **B662** (2008) 117–122 [0706.3059].

[60] J. F. Gunion and G. Bertsch, Phys. Rev. **D25** (1982) 746.

[61] B. Z. Kopeliovich, J. Nemchik and I. Schmidt, Nucl. Phys. **A782** (2007) 224–233 [hep-ph/0608044].

[62] A. Deshpande, "Physics and status of the Electron-Ion Collider (EIC)", talk at PANIC08 (13 Nov 2008) [http://www.weizmann.ac.il/MaKaC/conferenceDisplay.py?confId=0].

[63] A. Deshpande, "Summary of the discussion at ECT* Trento on Staged Realization of the EIC (eRHIC)" (14-18 Jul 2008) [http://www.eic.bnl.gov/TrentoJuly08/EIC-Trento-Talks/Day-5-Talks/].

[64] J. B. Dainton, M. Klein, P. Newman, E. Perez and F. Willeke, JINST **1** (2006) P10001 [hep-ex/0603016].

[65] D. von Harrach, "MANUEL@FAIR: a design study for a polarized e-p collider at FAIR", talk (25 Sep 2008) [http://www.jlab.org/ ent/ELIC/v.harrach.gsiep.pdf].